Electronic Supplementary Information

In situ controllably self-assembled amorphous Co-TDPAT MOFs as superior cocatalysts of α-Fe_2O_3 nanosheet arrays for highly efficient and ultrastable photoelectrochemical oxygen evolution

Weiguang Hu [a,b,c], Qinghua Xia [c], Lian Ying Zhang [d], Jianguo Lu [e], Qinggang He [b], Weiyong Yuan [b,c,*]

[a] *School of Biological and Chemical Engineering, NingboTech University, Ningbo 315100, China*

[b] *College of Chemical and Biological Engineering, Zhejiang University, Hangzhou 310027, China*

[c] *Ningbo Innovation Centre, Zhejiang University, Ningbo 315100, China*

[d] *College of Materials Science and Engineering, Qingdao University, Qingdao 266071, China*

[e] *State Key Laboratory of Silicon Materials, School of Materials Science and Engineering, Zhejiang University, Hangzhou 310027, China*

* *Corresponding author. E-mail address: wyyuan@zju.edu.cn*

Contents

11. XRD patterns of Co-TDPAT grown on α-Fe_2O_3 NSA for 20, 40, and 60 min (Figure S7).

12. High-resolution Co 2p XPS spectra of Co-TDPAT grown on α-Fe_2O_3 NSA for 20, 40, and 60 min (Figure S8).

13. Photocurrent densities and maximum photoconversion efficiencies of representative FTO supported α-Fe_2O_3 NSA-based photoanodes for water splitting (Table S1).

14. Onset potentials and stability of representative FTO supported α-Fe_2O_3-based photoanodes in 1 M NaOH/KOH (Table S2).

15. High-resolution Fe 2p XPS spectra of α-Fe_2O_3 NSA before and after growth of Co-TDPAT (Figure S9).

16. Valence band and the secondary electron onset position of α-Fe_2O_3 NSA and α-Fe_2O_3 NSA@a-Co-TDPAT (Figure S10).

17. FESEM images of α-Fe_2O_3 NSA@a-Co-TDPAT before and after the stability test (Figure S11).

18. XRD patterns of α-Fe_2O_3 NSA@a-Co-TDPAT before and after the stability test (Figure S12).

19. High-resolution Co 2p XPS spectra of α-Fe_2O_3 NSA@a-Co-TDPAT before and after the stability test (Figure S13).

1. Calculation of photoconversion efficiency

The photoconversion efficiency of a photoanode was calculated according to the following formula [1,2]:

$$\eta\% = \frac{J(1.23 - V)}{P} \times 100$$

Where J is the current density under simulated sunlight irradiation, V is the applied voltage versus RHE, and P is the light intensity (100 mW cm^{-2}).

2. Calculation of donor density

N_d can be estimated from the slope of the M-S plots according to the following equation [1,3]:

$$N_d = \frac{2}{e_0 \varepsilon \varepsilon_0}\left[\frac{d\frac{1}{C^2}}{dV}\right]^{-1}$$

where e_0 is the electron charge, ε the dielectric constant of $\alpha\text{-}Fe_2O_3$, ε_0 the permittivity of vacuum (8.85×10^{-12} N^{-1} C^2 m^{-2}).

3. Calculation of Debye length

The charge carrier diffusion lengths (Debye length, L_D) for both electrodes were also calculated according to the following equation [1,4]:

$$L_D = \left(\frac{\varepsilon \varepsilon_0 kT}{e^2 N_D}\right)^{\frac{1}{2}}$$

where k is the Boltzmann constant (1.38×10^{-23} J K^{-1}) and T is the absolute temperature (K).

4. Calculation of depletion layer width

The depletion layer width (W) at 1.0 V vs. RHE can be calculated via the following equation [1,4]:

$$W = \left(\frac{2\varepsilon \varepsilon_0 \phi}{e^2 N_D}\right)^{\frac{1}{2}}$$

where $\phi = V - V_{FB}$ is the maximum potential drop in the depletion layer.

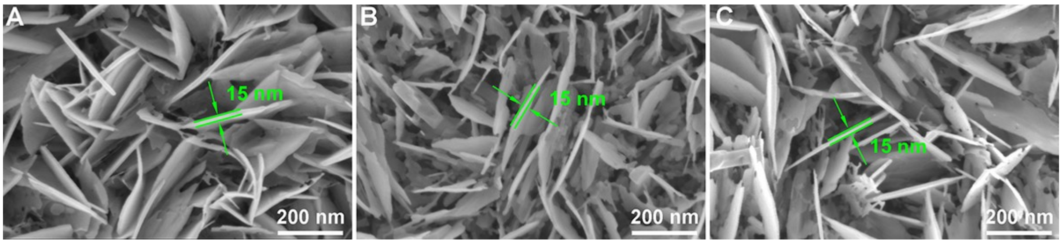

Figure S1. FESEM images of α-Fe_2O_3 NSA before the hydrothermal reaction (A) and after hydrothermal reactions with only H_6TDPAT (B) and with only Co^{2+} (C) in solution.

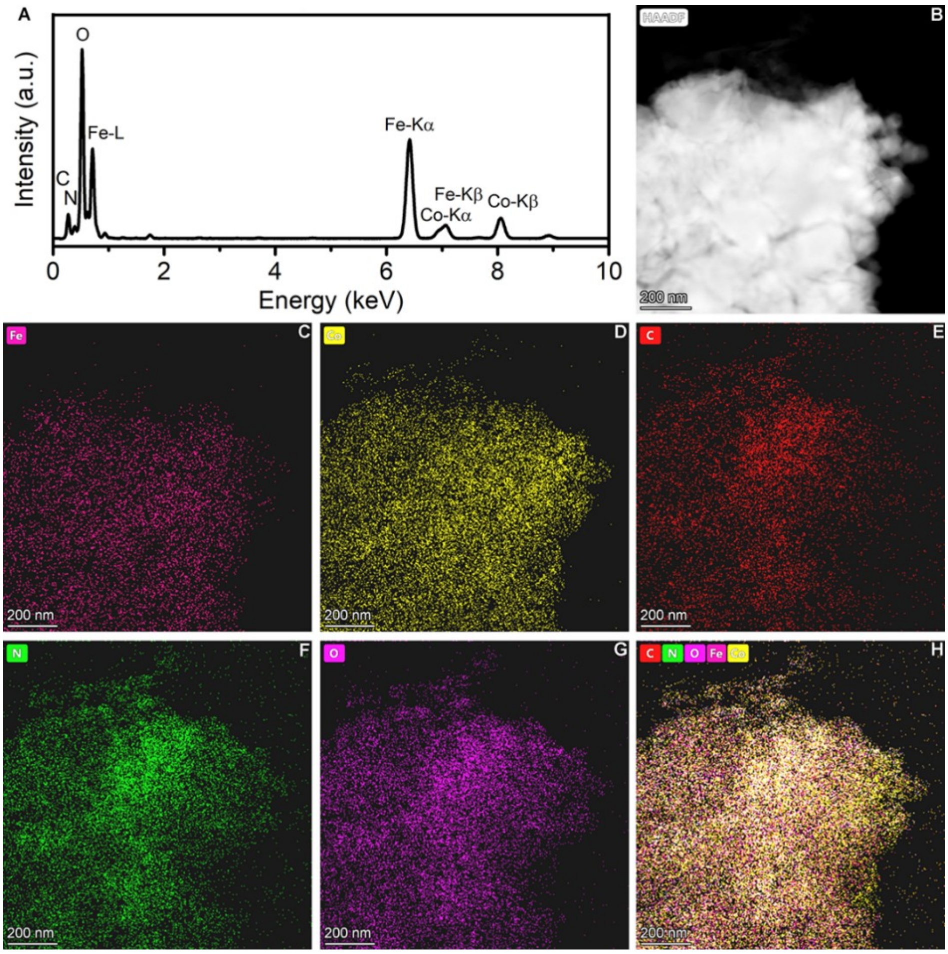

Figure S2. EDX spectrum (A), HADDF-STEM image (B), and EDS mapping images (C-H) of α-Fe_2O_3 NSA@a-Co-TDPAT. (C), (D), (E), (F), and (G) show the distribution of Fe, Co, C, N, and O, respectively, and (H) shows the overlapping image of C, N, O, Fe, and Co.

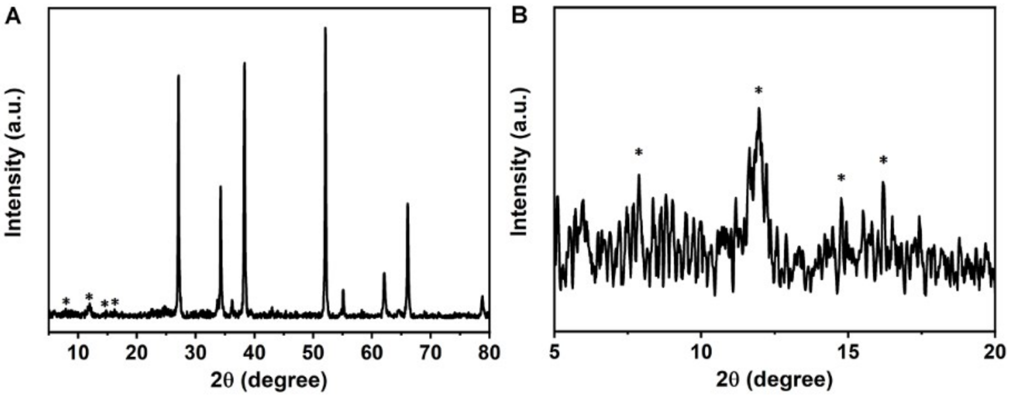

Figure S3. XRD pattern (A) and enlarged XRD pattern (B) of Co-TDPAT grown on α-Fe_2O_3 NSA (the growth time is 60 min).

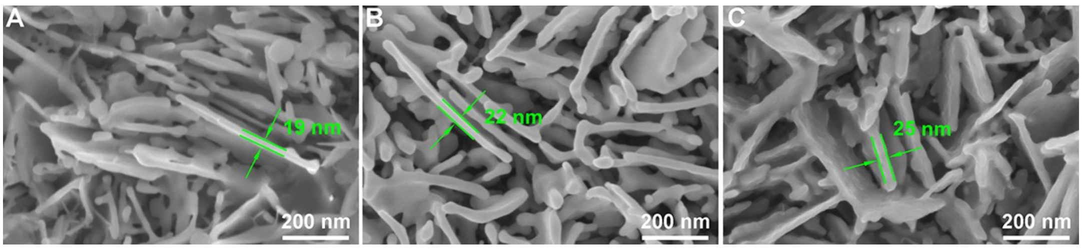

Figure S4. FESEM images of Co-TDPAT grown on α-Fe_2O_3 NSA at 80 ˚C (A), 120 ˚C (B), and 160 ˚C (C).

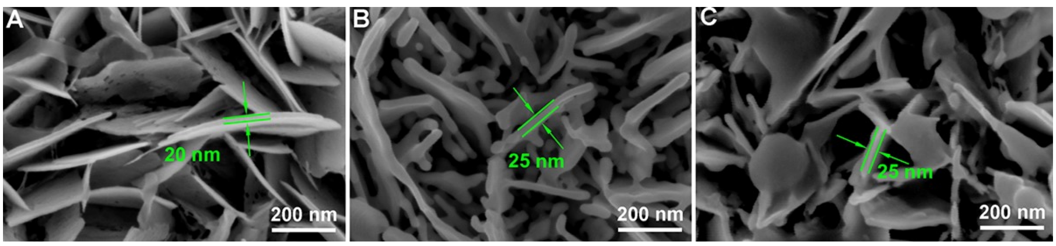

Figure S5. FESEM images of Co-TDPAT grown on α-Fe_2O_3 NSA using Co^{2+} concentrations of 2 (A), 10 (B), and 50 (C) mM.

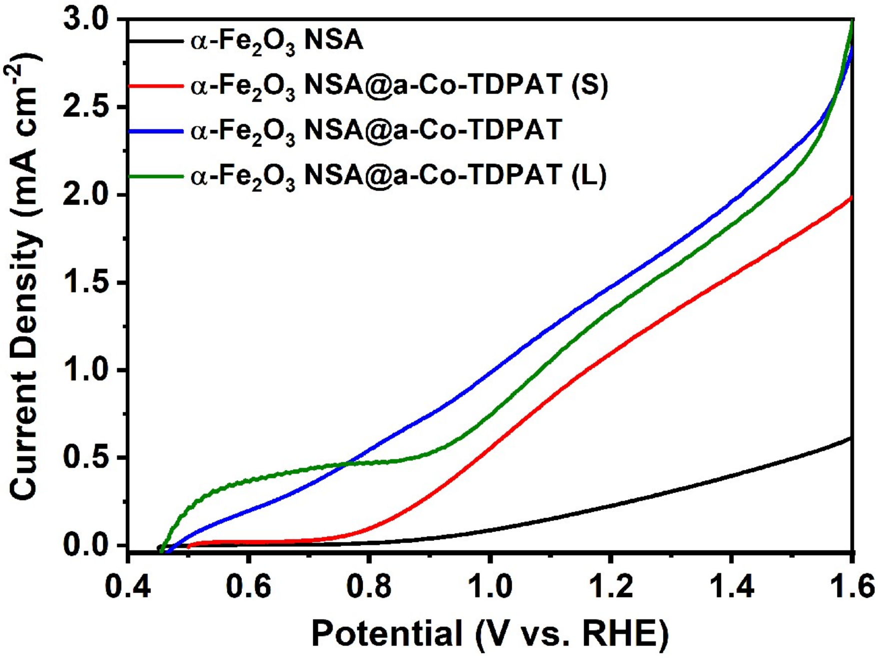

Figure S6. Linear sweep voltammograms of α-Fe_2O_3 NSA, Fe_2O_3 NSA@a-Co-TDPAT (S), Fe_2O_3 NSA@a-Co-TDPAT, and α-Fe_2O_3 NSA@a-Co-TDPAT (L).

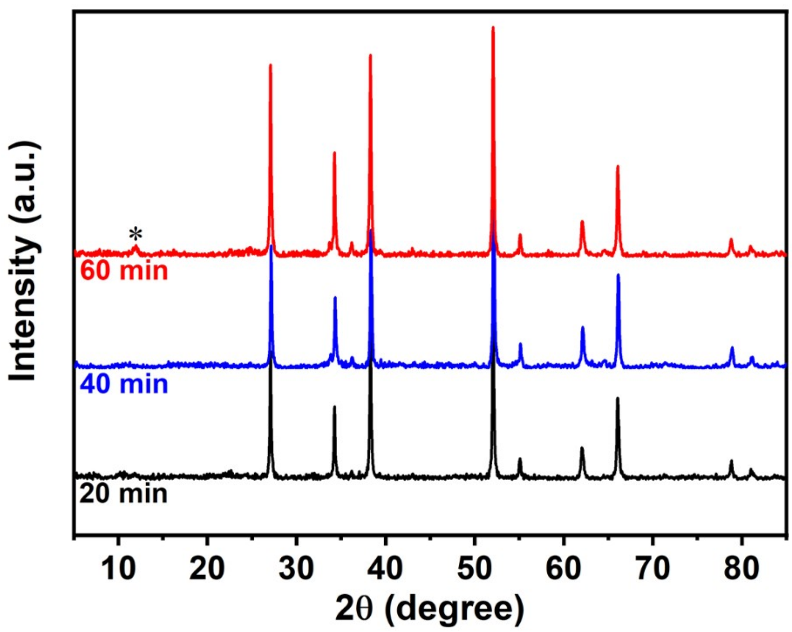

Figure S7. XRD patterns of Co-TDPAT grown on α-Fe_2O_3 NSA for 20, 40, and 60 min. The peak labeled with "*" is due to crystallization of the Co-TDPAT MOF.

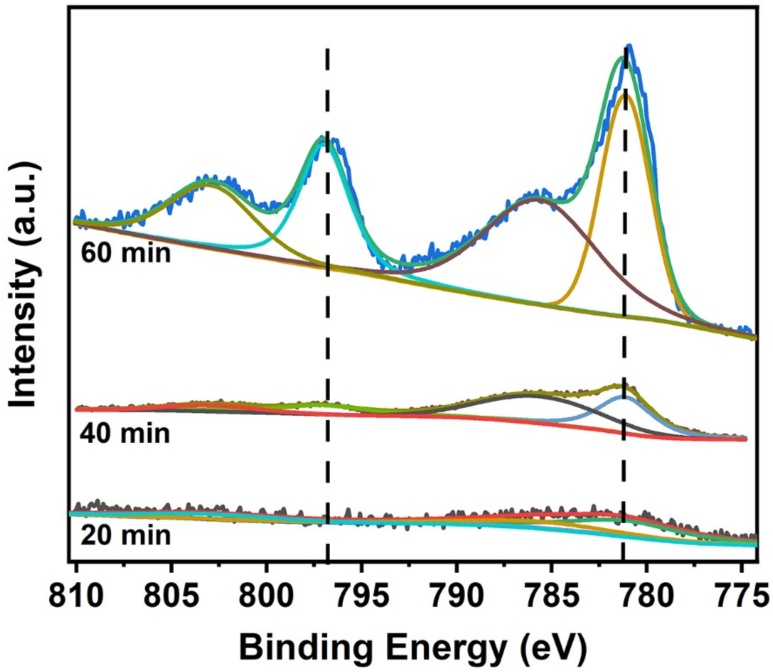

Figure S8. High-resolution Co 2p XPS spectra of Co-TDPAT grown on α-Fe_2O_3 NSA for 20, 40, and 60 min.

Table S1. Photocurrent densities and maximum photoconversion efficiencies of representative FTO-supported α-Fe_2O_3 NSA-based photoanodes for water splitting in 1.0 M NaOH/KOH (Light source used: AM 1.5 G, 100 mW cm^{-2}).

Photoanode	Photocurrent density (V vs. RHE)	Maximum photoconversion efficiency	Reference
Zr-doped α-Fe_2O_3 16 h synthesis	0.52 (1.5V)	N.A.	5
Fe_2O_3 nanoplates	~0.0567 (1.23)	N.A.	6
P-Fe_2O_3	0.78 (1.23)	0.085%	7
P-Fe_2O_3/Ce-Pi	1.24 (1.23)	N.A.	7
Fe_2O_3/C_3N_4/CoO_x	1.50 (1.23)	0.17%	8
In treated α-Fe_2O_3	0.65 (1.23)	~0.055%	9
In treated α-Fe_2O_3/Co-Pi	~1 (1.23)	N.A.	9
Sn-Fe_2O_3/CoPi	0.6 (1.23)	N.A.	10
α-Fe_2O_3 NSA-Ti	0.77 (1.23)	N.A.	11
Ge-doped α-Fe_2O_3 nanosheet arrays (500)	1.4 (1.23)	N.A.	12
α-Fe_2O_3	0.53 (1.23)	N.A.	13
Sn-doped hematite (5%)	1.51 (1.23)	N.A.	14
Ge-doped hematite (6%)	0.42 (1.23)	N.A.	14
2at.%Co-Fe-1 at.%Ca	0.095 (1.23)	N.A.	15

α-Fe_2O_3 NSA@a-Co-TDPAT	**~1.54 (1.23)**	**0.25%**	**This work**

Table S2. Onset potentials and stability of representative FTO-supported α-Fe_2O_3-based photoanodes in 1 M NaOH/KOH (Light source used: AM 1.5 G, 100 mW cm^{-2}).

Photoanode	**Onset potential (V vs. RHE)**	**Stability (1.23V vs. RHE)**	**Reference**
P-Fe_2O_3/Ce-Pi	0.72	5.5	7
Fe_2O_3/C_3N_4/CoO_x	0.62	5	8
Sn-Fe_2O_3/CoPi	0.65	0.167	10
Ge-doped hematite (6%)	~0.67	N.A.	14
2at.%Co-Fe-1 at.%Ca	0.6	N.A.	15
Ni-MOF/Fe_2O_3-24h	0.61	2	16
Cu@α-Fe_2O_3-Vo-pn-1mM-4h	0.736	3	17
$NiCo(OH)_x$/BCN/F	0.6	5	18
S-FeOOH@Fe_2O_3	0.58	5	19
0.02 M Li@α-Fe_2O_3	0.6	N.A.	20
Co-Pi/Co_3O_4/Ti:Fe_2O_3	0.64	0.1	21
FTO/p-Fe_2O_3/Fe-Pi/$ZnFe_2O_3$	0.7	N.A.	22
$Ni(OH)_2$ QDs/α-Fe_2O_3	0.71	2	23
Fe_2O_3@ZIF-67-0.75	0.74	2	24
Co-Pi/Fe_2O_3-$NaBH_4$	0.7	12	25
CoP/SnO_2:Fe_2O_3	0.81	5	26
3-Si/Ti:HT	0.8	8	27
α-Fe_2O_3/rGO/NiFe-LDH	0.65	2	28
Ni_2P/Ta:α-Fe_2O_3	0.68	24	29
Pristine α-Fe_2O_3	0.7	N.A.	30
CoO_x@C/Ti-Fe_2O_3	0.611	2	31
Ce-Fe_2O_3/ZIF-67	0.639	3	32
2h FeOOH/Fe_2O_3	0.582	5	33
Grey hematite	0.61	N.A.	34
WN-α-Fe_2O_3@Co_3O_4/GQD	0.72	2	35
Ti-Fe_2O_3/$NiFeS_x$	0.79	N.A.	36
Ti_i-Pt_i	0.7	N.A.	37
WN-α-Fe_2O_3@Co_3O_4	0.62	2	38
Co-Ci/Zr-Fe_2O_3(LV)	0.85	20	39
Fe_2O_3/Fe_2TiO_5/LDH	~0.84	20	40
Ta:Fe_2O_3@$CaFe_2O_4$/$FeNiO_x$	0.63	50	41
FeCo-MOF/F	0.8	5	42
Zn-doped α-Fe_2O_3	0.6	2.3	43
HEDP-Fe_2O_3/Fe_2TiO_5/FeNiOOH	0.64	N.A.	44
Ti-Fe_2O_3	~0.8	4	45
0FeP/Ti-Fe_2O_3	0.88	N.A.	46
FTO/TiO_2/Sn@α-Fe_2O_3/Co-Pi	0.71	10	47
CoOOH/Fe_2O_3	0.75	2	48
HfFe-NP	0.67	10	49
Co-MOF/Ti:Fe_2O_3	0.61	6	50
Mo/Sn codoped α-Fe_2O_3	0.68	N.A.	51

F-Ti-Fe_2O_3/FeNiOOH	0.57	N.A.	52
ATO-Fe_2O_3	~0.86	N.A.	53
$NiFeO_x$/P,Ti-Fe_2O_3	~0.73	20	54
Co-Pi/MNs/α-Fe_2O_3	0.57	20	55
α-Fe_2O_3/Co(salen)-250	0.6	3	56
W-Zr-Fe_2O_3	0.61	N.A.	57
exfLDH/α-Fe_2O_3	0.55	N.A.	58
Co-Sil/F-Fe_2O_3	0.7	5	59
Fe_2O_3/TiO_2/FeNiOOH	0.61	N.A.	60
2D SnO_2/Fe_2O_3	~0.65	0.083	61
α-Fe_2O_3/CoPi	0.65	12	62
Ni-Bi/Ti-Fe_2O_3	0.85	6	63
1ZnFe-H	0.98	1	64
Fe_2O_3/Sn-10/NiO_x	0.65	24	65
FeFx/Zr-Fe_2O_3	0.77	3	66
PC-Fe_2O_3	0.55	N.A.	67
6W-TiO_2/Ti-Fe_2O_3	0.88	N.A.	68
Fe_2O_3 NT-FeOOH/NiOOH	~0.66	4	69
α-Fe_2O_3-2c-Fe(II) LA	0.58	3	70
FTO/Sn@α-Fe_2O_3/NiOOH−Ar	0.71	10	71
Fe_2O_3-$Co(OH)_2$	0.85	6	72
CoMo-Fe_2O_3(LV)	0.72	1	73
Ti-Fe_2O_3/In_2O_3	~0.8	3	74
$FePO_4 \cdot 2H_2O$	0.74	0.5	75
Hematite nanowires	0.8	N.A.	76
α-Fe_2O_3 NSA@a-Co-TDPAT	**~0.48**	**24**	**This work**

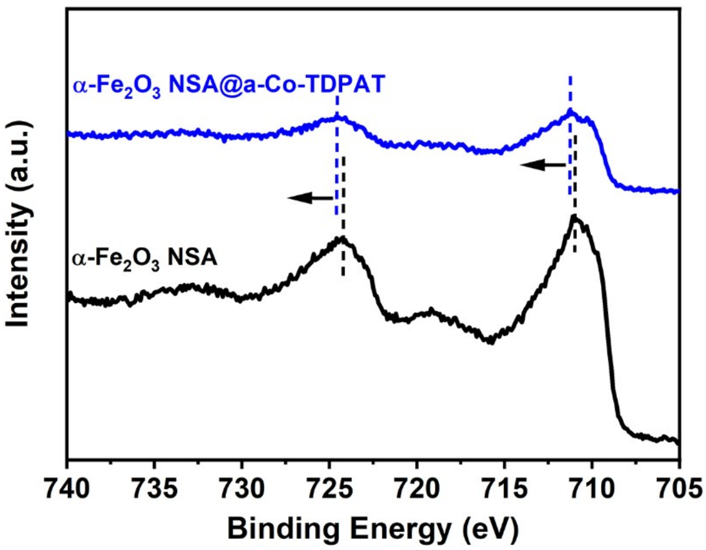

Figure S9. High-resolution Fe 2p XPS spectra of α-Fe_2O_3 NSA before and after growth of Co-TDPAT.

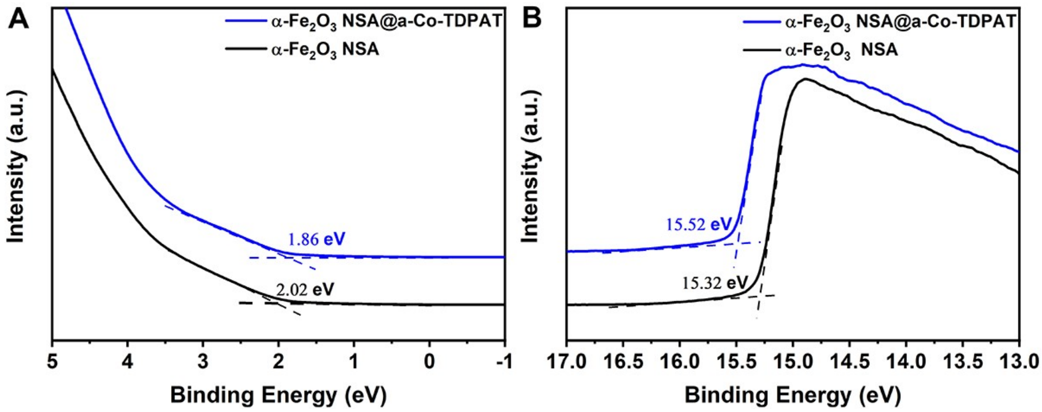

Figure S10. Valence band (A) and the secondary electron onset position (B) of α-Fe_2O_3 NSA and α-Fe_2O_3 NSA@a-Co-TDPAT. The valence band value of α-Fe_2O_3 NSA equals (21.2-15.32+2.02) eV, which is 7.9 eV and that of α-Fe_2O_3 NSA@a-Co-TDPAT equals (21.1-15.52+1.86) eV, which is 7.44 eV.

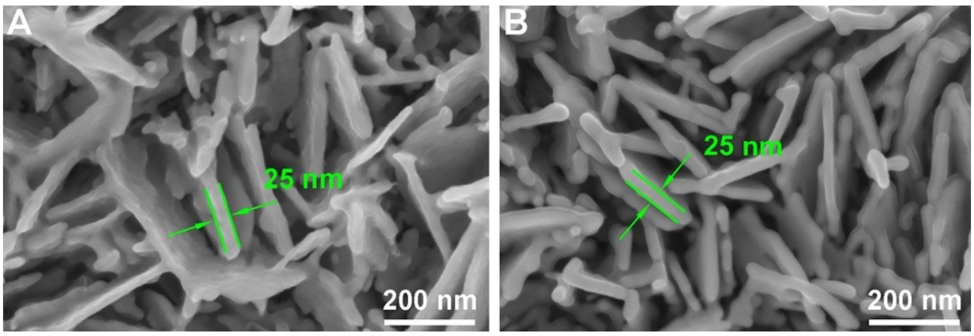

Figure S11. FESEM images of α-Fe_2O_3 NSA@a-Co-TDPAT before (A) and after (B) the stability test.

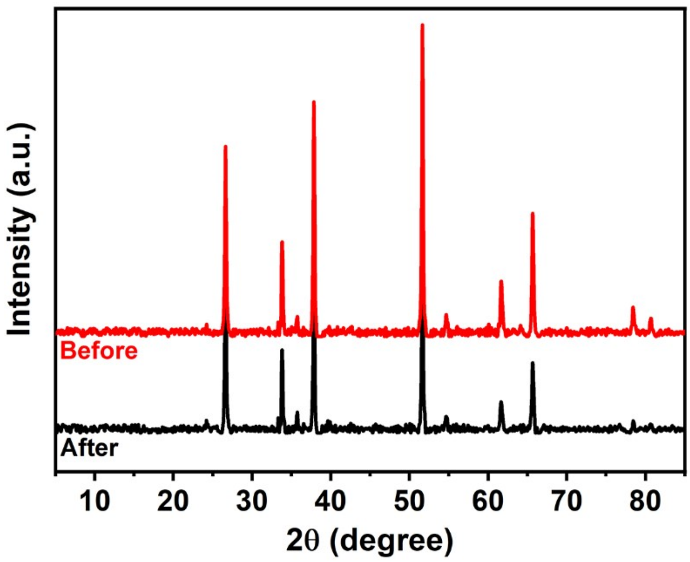

Figure S12. XRD patterns of α-Fe_2O_3 NSA@a-Co-TDPAT before (A) and after (B) the stability test.

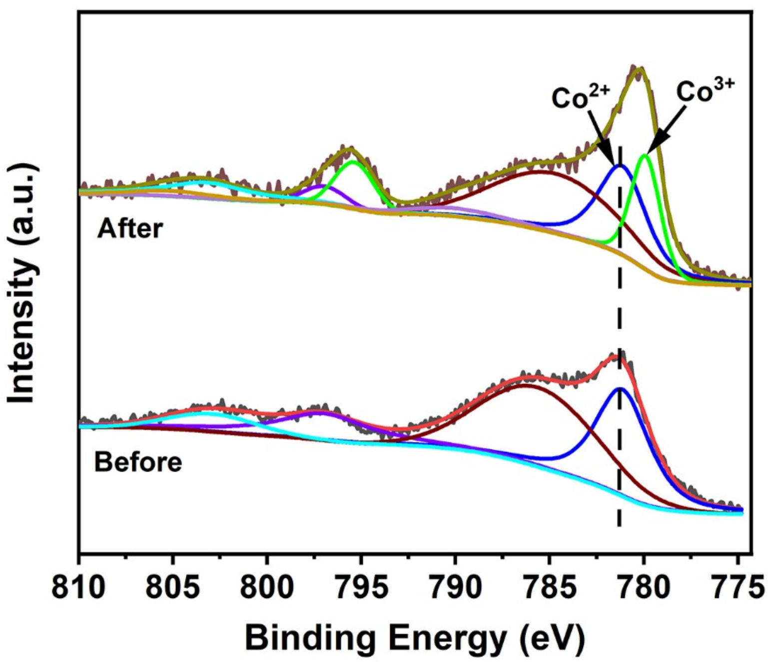

Figure S13. High-resolution Co 2p XPS spectra of α-Fe_2O_3 NSA@a-Co-TDPAT before (A) and after (B) the stability test.

References

[1] W. Yuan, J. Yuan, J. Xie, C.M. Li, Polymer-mediated self-assembly of TiO_2@Cu_2O core-shell nanowire array for highly efficient photoelectrochemical water oxidation, ACS Appl. Mater. Interfaces 8 (2016) 6082–6092.

[2] Z. Li, W. Luo, M. Zhang, J. Feng, Z. Zou, Photoelectrochemical cells for solar hydrogen production: current state of promising photoelectrodes, methods to improve their properties, and outlook, Energy Environ. Sci. 6 (2013) 347–370.

[3] K. Gelderman, L. Lee, S. W. Donne, Flat-band potential of a semiconductor: using the Mott-Schottky equation, J. Chem. Educ. 84 (2007) 685–688.

[4] C. Fàbrega, D. Monllor-Satoca, S. Ampudia, A. Parra, T. Andreu, J. R. Morante, Tuning the fermi level and the kinetics of surface states of TiO_2 nanorods by means of ammonia treatments, J. Phys. Chem. C 117 (2013) 20517–20524.

[5] B. Jansi Rani, M. Praveen Kumar, G. Ravi, S. Ravichandran, R. K. Guduru, R. Yuvakkumar, Electrochemical and photoelectrochemical water oxidation of solvothermally synthesized Zr-doped α-Fe_2O_3 nanostructures, Appl. Surf. Sci. 471 (2019) 733–744.

[6] F. Lei, H. Liu, J. Yu, Z. Tang, J. Xie, P. Hao, G. Cui, B. Tang, Promoted water splitting by efficient electron transfer between Au nanoparticles and hematite nanoplates: a theoretical and experimental study, Phys. Chem. Chem. Phys. 21 (2019) 1478–1483.

[7] X. Bu, Y. Gao, S. Zhang, Y. Tian, Amorphous cerium phosphate on P-doped Fe_2O_3 nanosheets for efficient photoelectrochemical water oxidation, Chem. Eng. J. 355 (2019) 910–919.

[8] Z. Mei, Y. Li, X. Yang, W. Ren, S. Tong, N. Zhang, W. Zhao, Y. Lin, F. Pan, Tuning nanosheet Fe_2O_3 photoanodes with C_3N_4 and p-type CoO: X decoration for efficient and stable water splitting, Catal. Sci. Technol. 8 (2018) 3144–3150.

[9] X. Bu, G. Wang, Y. Tian, Foreign In^{3+} treatment improving the photoelectrochemical performance of a hematite nanosheet array for water splitting, Nanoscale 9 (2017) 17513–17523.

[10] J. Wang, J. Su, L.Guo, Controlled aqueous growth of hematite nanoplate arrays directly on transparent conductive substrates and their photoelectrochemical Propertie, Chem. Asian J. 11 (2016) 2328-2334.

[11] M. Ji, J. Cai, Y. Ma, L. Qi, Controlled growth of ferrihydrite branched nanosheet arrays and their transformation to hematite nanosheet arrays for photoelectrochemical water splitting, ACS Appl. Mater. Interfaces 8 (2016) 3651–3660.

[12] J. Liu, Y. Y. Cai, Z. F. Tian, G. S. Ruan, Y. X. Ye, C. H. Liang, G. S. Shao, Highly oriented Ge-doped hematite nanosheet arrays for photoelectrochemical water oxidation, Nano Energy 9 (2014) 282–290.

[13] M. Marelli, A. Naldoni, A. Minguzzi, M. Allieta, T. Virgili, G. Scavia, S. Recchia, R. Psaro, V. Dal Santo, Hierarchical hematite nanoplatelets for photoelectrochemical water splitting, ACS Appl. Mater. Interfaces 6 (2014) 11997–12004.
[14] S. Li, J. Cai, Y. Mei, Y. Ren, G. Qin, Thermal oxidation preparation of doped hematite thin films for photoelectrochemical water splitting, Int. J. Photoenergy 2014 (2014) 794370.
[15] J. Cai, S. Li, G. Qin, Interface engineering of Co_3O_4 loaded $CaFe_2O_4/Fe_2O_3$ heterojunction for photoelectrochemical water oxidation, Appl. Surf. Sci. 466 (2019) 92–98.
[16] X. Liu, F. Zhan, D. Li, M. Xue, α-Fe_2O_3 nanoarrays photoanodes decorated with Ni-MOFs for enhancing photoelectrochemical water oxidation, Int. J. Hydrogen Energy 45 (2020) 28836–28846.
[17] H. Wang, Y. Hu, G. Song, D. Zheng, Intrinsic and extrinsic doping to construct hematite nanorod p-n homojunctions for highly efficient PEC water splitting, Chem. Eng. J. 435 (2022) 135016.
[18] Z. Zhang, T. Yang, Z. Wang, H. Wang, X. Yue, S. Yi, Extremely low onset potential of modified Fe_2O_3 photoanode for water oxidation, Appl. Surf. Sci. 642 (2024) 158597.
[19] N. D. Quang, P. C. Van, S. Majumder, J. Jeong, D. Kim, C. Kim, Rational construction of S-doped FeOOH onto Fe_2O_3 nanorods for enhanced water oxidation, J. Colloid Interface Sci. 616 (2022) 749–758.
[20] J. Cai, L. Xu, X. Tang, L. Kong, J. Wang, R. Wang, X. Li, Q. Xie, K. Mao, H. Pan, Role of lithium doping on α-Fe_2O_3 photoanode for enhanced photoelectrochemical water oxidation, J. Alloys Compd. 915 (2022) 165349.
[21] S. S. Yi, B. R. Wulan, J. M. Yan, Q. Jiang, Highly efficient photoelectrochemical water splitting : surface modification of cobalt-phosphate-loaded Co_3O_4/Fe_2O_3 p–n heterojunction nanorod arrays, 29 (2019) 1801902.
[22] J. Li, H. Wang, Y. Li, S. Xue, Y. Wang, Hematite photoanodes decorated with a Zn-doped Fe_2O_3 catalyst for efficient photoelectrochemical water oxidation, Int. J. Electrochem. Sci. 17 (2022) 22106.
[23] J. Rong, Z. Wang, J. Lv, M. Fan, R. Chong, Z. Chang, $Ni(OH)_2$ quantum dots as a stable cocatalyst modified α-Fe_2O_3 for enhanced photoelectrochemical water-splitting, Chinese J. Catal. 42 (2021) 1999–2009.
[24] W. Li, K. Wang, X. Yang, F. Zhan, Y. Wang, M. Liu, X. Qiu, Surfactant-assisted controlled synthesis of a metal-organic framework on Fe_2O_3 nanorod for boosted photoelectrochemical water oxidation, Chem. Eng. J. 379 (2020) 122256.
[25] J. Xiao, L. Fan, F. Zhao, Z. Huang, S. Zhou, G. Zhan, Kinetic analysis of the synergistic effect of $NaBH_4$ treatment and Co-Pi coating on Fe_2O_3 photoanodes for photoelectrochemical water oxidation, J. Catal. 381 (2020) 139–149.
[26] N. D. Quang, W. Hu, H. S. Chang, P. C. Van, D. D. Viet, J. R. Jeong, D. B. Seo, E. T.

Kim, C. Kim, D. Kim, Fe_2O_3 hierarchical tubular structure decorated with cobalt phosphide (CoP) nanoparticles for efficient photoelectrochemical water splitting, Chem. Eng. J. 417 (2021) 129278.

[27] T. S. Koh, P. Anushkkaran, W. S. Chae, H. H. Lee, S. H. Choi, J. S. Jang, Gradient Si- and Ti-doped Fe_2O_3 hierarchical homojunction photoanode for efficient solar water splitting: Effect of facile microwave-assisted growth of Si-FeOOH on Ti-FeOOH nanocorals, J. Energy Chem. 77 (2023) 27–37.

[28] Y. Liu, X. Li, R. Mo, P. Xie, M. Yin, H. Li, Enhancing the photoelectrochemical water oxidation activity of α-Fe_2O_3 thin film photoanode by employing rGO as electron transfer mediator and NiFe-LDH as Cocatalyst, ChemCatChem 13 (2021) 4729–4737.

[29] X. Cao, P. Wen, R. Ma, Y. Liu, S. Sun, Q. Ma, P. Zhang, Y. Qiu, Ni_2P nanocrystals modification on Ta:α-Fe_2O_3 photoanode for efficient photoelectrochemical water splitting: In situ formation and synergistic catalysis of Ni_2P@NiOOH cocatalyst, Chem. Eng. J. 449 (2022) 137792.

[30] Y. Wang, J. Liu, J. Xu, X. Hao, Effect of acid treatment on boosting the photoelectrochemical performance of doped and codoped α-Fe_2O_3 photoanodes, RSC Adv. 13 (2023) 16765–16772.

[31] H. Li, K. Ba, K. Zhang, Y. Lin, W. Zhu, T. Xie, Facile synthesis of CoO_x@C/Ti-Fe_2O_3 photoanodes for efficient photoelectrochemical water oxidation, Dalt. Trans. 53 (2023) 115–122.

[32] J. Wu, J. Liu, L. Jin, B. Hu, W. Liu, Hybrid Ce-Fe_2O_3/ZIF-67 Photoanode with efficient photoelectrochemical water oxidation performance, Inorg. Chem. 61 (2022) 12591–12598.

[33] Y. Wei, A. Liao, L. Wang, X. Wang, D. Wang, Y. Zhou, Z. Zou, Room temperature surface modification of ultrathin FeOOH cocatalysts on Fe_2O_3 photoanodes for high photoelectrochemical water splitting, J. Nanomater. 2020 (2020) 7148714.

[34] P. F. Liu, C. Wang, Y. Wang, Y. Li, B. Zhang, L. R. Zheng, Z. Jiang, H. Zhao, H. G. Yang, Grey hematite photoanodes decrease the onset potential in photoelectrochemical water oxidation, Sci. Bull. 66 (2021) 1013–1021.

[35] C. Li, S. Ma, M. Zhao, M. Jing, W. Yuan, C. Li, Self-assembled α-Fe_2O_3@Co_3O_4/graphene quantum dot core-hybrid shell wormlike nanoarrays with synergistic effects for photoelectrochemical water oxidation, ACS Sustain. Chem. Eng. 11 (2023) 12102–12113.

[36] H. Wang, R. Zhang, Y. Y. Li, D. Wang, Y. Lin, T. Xie, Simple electrodeposition to synthesize a $NiFeS_x$-modified Ti-Fe_2O_3 photoanode: an effective strategy to improve the photoelectrochemical water oxidation reaction, Dalt. Trans. 50 (2021) 15551–15557.

[37] Z. Zhong, G. Zhan, B. Du, X. Lu, Z. Qin, J. Xiao, Design of Ti-Pt Co-doped α-Fe_2O_3 photoanodes for enhanced performance of photoelectrochemical water splitting, J. Colloid

Interface Sci. 641 (2023) 91–104.
[38] C. Li, Z. Chen, W. Yuan, Q. H. Xu, C. M. Li, In situ growth of α-Fe_2O_3@Co_3O_4 core-shell wormlike nanoarrays for a highly efficient photoelectrochemical water oxidation reaction, Nanoscale 11 (2019) 1111–1122.
[39] C. Li, C. Lu, Y. Zhu, S. Li, Y. Feng, Y. Yang, B. Xu, K. Feng, J. Zhong, In-situ electron capture by surface Co-Ci to facilitate the solar water splitting of Fe_2O_3, Chem. Eng. J. 486 (2024) 150120.
[40] J. C. N. Fouemina, G. Li, X. She, D. Yan, X. Lv, K. Nie, J. Deng, H. Xu, Surface self-transforming FeTi-LDH overlayer in Fe_2O_3/Fe_2TiO_5 photoanode for improved water oxidation, Small 19 (2023) 1–9.
[41] K. Kang, C. Tang, J. H. Kim, W. J. Byun, J. H. Lee, M. H. Lee, H. Zhang, J. S. Lee, In situ construction of Ta:Fe_2O_3@$CaFe_2O_4$ core-shell nanorod p-t-n heterojunction photoanodes for efficient and robust solar water oxidation, ACS Catal. (2023) 7002–7012.
[42] Z. Y. Wang, H. M. Li, S. S. Yi, M. Z. You, H. J. Jing, X. Z. Yue, Z. T. Zhang, D. L. Chen, In-situ coating of multifunctional FeCo-bimetal organic framework nanolayers on hematite photoanode for superior oxygen evolution, Appl. Catal. B Environ. 297 (2021) 120406.
[43] J. Cai, X. Tang, L. Xu, H. Li, H. Zhu, X. Li, Q. Xie, K. Mao, S. Li. Accelerated oxygen evolution kinetics on hematite by Zn^{2+} for boosting the photoelectrochemical water oxidation, J. Alloys Compd. 919 (2022) 165853.
[44] J. Deng, Y. Li, Y. Xiao, K. Feng, C. Lu, K. Nie, X. Lv, H. Xu, J. Zhong, Improved water oxidation of Fe_2O_3/Fe_2TiO_5 photoanode by functionalizing with a hydrophilic organic hole storage overlayer, ACS Catal. 12 (2022) 7833–7842.
[45] F. Feng, C. Li, J. Jian, F. Li, Y. Xu, H. Wang, L. Jia, Gradient Ti-doping in hematite photoanodes for enhanced photoelectrochemical performance, J. Power Sources 449 (2020) 227473.
[46] Q. Bu, S. Li, Q. Wu, Y. Lin, D. Wang, X. Zou, T. Xie, In situ synthesis of FeP-decorated Ti-Fe_2O_3: an effective strategy to improve the interfacial charge transfer in the photoelectrochemical water oxidation reaction, Catal. Sci. Technol. 9 (2019) 5812–5818.
[47] Z. Zhou, Y. Liang, X. S. Xing, K. Zhang, Y. Niu, L. Yang, F. Wang, Z. Guo, H. Song, S. Wu, Integration of cobalt-phosphate catalyst and titanium dioxide interlayer in the hematite photoanodes to improve photoelectrochemical water splitting for hydrogen production, Adv. Compos. Hybrid Mater. 6 (2023) 1–12.
[48] R. Chong, Z. Wang, M. Fan, L. Wang, Z. Chang, L. Zhang, Hematite decorated with nanodot-like cobalt (oxy)hydroxides for boosted photoelectrochemical water oxidation, J. Colloid Interface Sci. 629 (2023) 217–226.
[49] Y. Fu, Y. R. Lu, F. Ren, Z. Xing, J. Chen, P. Guo, W. F. Pong, C. L. Dong, L. Zhao, S.

Shen, Surface electronic structure reconfiguration of hematite nanorods for efficient photoanodic water oxidation, Sol. RRL 4 (2020) 1–11.
[50] F. Wu, J. Xie, Y. You, Z. Zhao, L. Wang, X. Chen, P. Yang, Y. Huang, Cobalt metal-organic framework ultrathin cocatalyst overlayer for improved photoelectrochemical activity of Ti-doped hematite, ACS Appl. Energy Mater. 3 (2020) 4867–4876.
[51] J. Xiao, B. Du, S. Hu, J. Zhong, X. Chen, Y. Zhang, D. Cai, S.F. Zhou, G. Zhan, Simultaneously enhanced charge separation and transfer in cocatalyst-free hematite photoanode by Mo/Sn codoping, ACS Appl. Energy Mater. 4 (2021) 10368–10379.
[52] H. Ji, S. Shao, G. Yuan, C. Lu, K. Feng, Y. Xia, X. Lv, J. Zhong, H. Xu, J. Deng, Unraveling the role of Ti_3C_2 MXene underlayer for enhanced photoelectrochemical water oxidation of hematite photoanodes, J. Energy Chem. 52 (2021) 147–154.
[53] C. Li, D. Wang, N. Suzuki, C. Terashima, Y. Liu, A. Fujishima, X. Zhang, A coral-like hematite photoanode on a macroporous SnO_2: Sb substrate for enhanced photoelectrochemical water oxidation, Electrochim. Acta 360 (2020) 2–4.
[54] J. Kang, K. Y. Yoon, J. E. Lee, J. Park, S. Chaule, J. H. Jang, Meso-pore generating P doping for efficient photoelectrochemical water splitting, Nano Energy 107 (2023) 108090.
[55] G. Yang, S. Li, X. Wang, B. Ding, Y. Li, H. Lin, D. Tang, X. Ren, Q. Wang, S. Luo, J. Ye, A universal strategy boosting photoelectrochemical water oxidation by utilizing MXene nanosheets as hole transfer mediators, Appl. Catal. B Environ. 297 (2021) 120268.
[56] R. Wang, Y. Kuwahara, K. Mori, Y. Bu, H. Yamashita, Tunable surface modification of a hematite photoanode by a Co(salen)-based cocatalyst for boosting photoelectrochemical performance, Catal. Sci. Technol. 10 (2020) 1714–1723.
[57] H. Lan, J. Deng, J. Zhong, Boosting the performance of hematite photoanodes for solar water oxidation by synergistic W-incorporation and Zr-passivation, Int. J. Hydrogen Energy 44 (2019) 16436–16442.
[58] Y. Bin Park, J. H. Kim, Y. J. Jang, J. H. Lee, M. H. Lee, B. J. Lee, D. H. Youn, J. S. Lee, Exfoliated NiFe layered double hydroxide cocatalyst for enhanced photoelectrochemical water oxidation with hematite photoanode, ChemCatChem 11 (2019) 443–448.
[59] H. Chai, P. Wang, T. Wang, L. Gao, F. Li, J. Jin, Surface reconstruction of cobalt species on amorphous cobalt silicate-coated fluorine-doped hematite for efficient photoelectrochemical water oxidation, ACS Appl. Mater. Interfaces 13 (2021) 47572–47580.
[60] X. Lv, S. Shao, Y. Xiao, J. Deng, One-step in-situ formation of TiO_2 nanosheets interconnected hematite photoanode for enhanced water oxidation, Appl. Surf. Sci. 560 (2021) 150036.
[61] S. P. Ratnayake, J. Ren, B. J. Murdoch, J. Van Embden, D. E. Gómez, C. F. McConville, E. Della Gaspera, Nanostructured electrodes based on two-dimensional SnO_2 for photoelectrochemical water splitting, ACS Appl. Energy Mater. 5 (2022) 10359–10365.

[62] T. Katsuki, Z. N. Zahran, Y. Tsubonouchi, D. Chandra, N. Hoshino, M. Yagi, p-n junction formation between CoPi and α-Fe_2O_3 layers enhanced photo-charge separation and catalytic efficiencies for efficient visible-light-driven water oxidation, Sustain. Energy Fuels 7 (2023) 2910–2922.

[63] C. Liu, T. Zhang, D. Zhao, C. Zhang, G. Ou, H. Jin, Z. Chen, Ti-doped hematite films coupled with ultrathin nickel-borate layer as photoanode for enhanced photoelectrochemical water oxidation, J. Mater. Sci. Mater. Electron. 32 (2021) 7061–7072.

[64] L. Li, P. Liang, C. Liu, H. Zhang, N. Mitsuzaki, Z. Chen, Preparation of Zn-modified hematite from ZnFe alloy film for photoelectrochemical water splitting, J. Alloys Compd. 797 (2019) 222–230.

[65] A. B. Silva, C. D. F. da Silva, F. L. Souza, F. W. S. Lucas, F. H. B. Lima, All-electrochemically synthesized tin and nickel oxide-modified hematite as photo-electrocatalyst anodes for solar-driven water splitting, J. Catal. 391 (2020) 273–281.

[66] X. Zhao, C. Lu, S. Li, Y. Chen, G. Zhang, D. Zhang, K. Feng, J. Zhong, FeF_x and Fe_2ZrO_5 Co-modified hematite for highly efficient solar water splitting, J. Energy Chem. 69 (2022) 414–420.

[67] W. Y. Yu, D. K. Ma, D. P. Yang, X. G. Yang, Q. L. Xu, W. Chen. S. Huang, Highly efficient utilization of light and charge separation over hematite photoanode achieved through noncontact photonic crystal film for photoelectrochemical water splitting, Phys. Chem. Chem. Phys. 2 (2021) 1–5.

[68] L. Bi, X. Liang, W. Zhang, Z. Wu, J. Zhan, T. Xie, L. Zhang, W. Xu, J. Jiang, M. Wu, Improving the charge separation efficiency by embedding the electron transfer layer of hematite photoanode for photoelectrochemical water oxidation, Colloids Surf. A Physicochem. Eng. Aspects 683 (2024) 133103.

[69] C. Feng, S. Fu, W. Wang, Y. Zhang, Y. Bi, High-crystalline and high-aspect-ratio hematite nanotube photoanode for efficient solar water splitting, Appl. Catal. B Environ. 257 (2019) 117900.

[70] X. Liu, H. Wang, W. Qiu, Q. Wu, H. Wang, S. Xue, Dentritic hemaitite thinfilms with ferrous lactate overlayers for efficient photoelectrochemical water splitting, Sol. Energy 231 (2022) 897–907.

[71] Z. Zhou, F. Wang, P. Liang, L. Yang, Y. Yu, L. Li, Y. Guo, S. Wu, Reconstructing oxygen vacancies in the bulk and nickel oxyhydroxide overlayer to promote the hematite photoanode for photoelectrochemical water oxidation, ACS Appl. Energy Mater. 5 (2022) 8999–9008.

[72] S. Dadashi Radvar, A. Yourdkhani, R. Poursalehi, A facile route for decoration of hematite photoanodes by transition metal hydroxide co-catalysts, J. Am. Ceram. Soc. 107 (2024) 5178–5189.

[73] G. Zhang, C. Lu, C. Li, S. Li, X. Zhao, K. Nie, J. Wang, K. Feng, J. Zhong, $CoMoO_4$-modified hematite with oxygen vacancies for high-efficiency solar water splitting, Phys. Chem. Chem. Phys. 3 (2023) 13410–13416.
[74] Q. Zhao, P. Huang, D. Hu, T.B. Li, B. Xu, Passivation of hematite surface states to improve water wplitting performance, ChemPhotoChem 7 (2023) e202300013.
[75] F. Parveh, A. Yourdkhani, R. Poursalehi, Surface passivation of hematite photoanodes using iron phosphate, New J. Chem. 47 (2023) 15588–15598.
[76] Y. Wang, M. Rong, J. Zheng, Z. Rui, Morphology control of the hematite photoanodes for photoelectrochemical water splitting, Int. J. Hydrogen Energy 45 (2020) 31667–31677.